1 **Transient simulations of the present and the last**

2 **interglacial climate using the Community Climate**

3 **System Model version 3: effects of orbital acceleration**

4

5 **V. Varma[1, *], M. Prange[1, 2] and M. Schulz[1, 2]**

6

7 [1] {MARUM - Center for Marine Environmental Sciences, University of Bremen,

8 Germany}

9 [2] {Faculty of Geosciences, University of Bremen, Germany}

10 [*] {Now at: National Institute of Water and Atmospheric Research, Wellington, New

11 Zealand}

12

13 Correspondence to: V. Varma (vidya.varma@niwa.co.nz)

14

15

16

17

18

19

20

21

22

23

24

25

26

27

28

29

30

31

32

33

Abstract

Numerical simulations provide a considerable aid in studying past climates. Out of the various approaches taken in designing numerical climate experiments, transient simulations have been found to be the most optimal when it comes to comparison with proxy data. However, multi-millennial or longer simulations using fully coupled general circulation models are computationally very expensive such that acceleration techniques are frequently applied. In this study, we compare the results from transient simulations of the present and the last interglacial with and without acceleration of the orbital forcing, using the comprehensive coupled climate model CCSM3 (Community Climate System Model 3). Our study shows that in low-latitude regions, the simulation of long-term variations in interglacial surface climate is not significantly affected by the use of the acceleration technique (with an acceleration factor 10) and, hence, large-scale model-data comparison of surface variables is not hampered. However, in high-latitude regions where the surface climate has a direct connection to the deep ocean, e.g. in the Southern Ocean or the Nordic Seas, acceleration-induced biases in sea-surface temperature evolution may occur with potential influence on the dynamics of the overlying atmosphere.

1 Introduction

Earth's past climate is simulated numerically through either equilibrium simulations ("time slice experiments") or through transient simulations with time-dependent boundary conditions using climate models. In equilibrium simulations, the boundary conditions are not varied temporally but rather kept fixed under the assumption that the Earth system is in equilibrium with them (e.g. Braconnot et al., 2007; Lunt et al., 2013; Milker et al., 2013; Rachmayani et al., 2016). Evidently, only limited information regarding the temporal evolution of the dynamic system is obtained by the time slice approach. This approach significantly reduces the computational expenses for the otherwise 'costly' multi-millennial or longer transient simulations, which involve temporally varying boundary conditions.

Another approach to bypass the expensive transient simulations using coupled general circulation models (CGCMs) is by using Earth System Models of Intermediate Complexity (EMICs), which describe the dynamics of the atmosphere and/or ocean with simplified physics. EMICs are simple enough to allow long-term climate simulations over several thousands of years or even glacial cycles prescribing or

2

68 parameterizing many of the dynamical processes that are explicitly resolved in
69 CGCMs (Claussen et al., 2002). However, in studies that require more realistic
70 simulation of physical processes and high spatial resolution the use of comprehensive
71 CGCMs is inevitable.

72 When it comes to comparison of the model results with proxy data, transient
73 simulations give a superior insight compared to time slice experiments, since all of the
74 available data (time series) can be used, whereas model-data comparison with time-
75 slice experiments makes use of only a small fraction of all available data. This also
76 implies that transient simulations allow the application of the whole spectrum of
77 statistical methods for spatio-temporal data analysis for model-data comparison, thus
78 offering a much stronger assessment of the model performance as well as the data
79 quality (e.g. Liu et al., 2014; Otto-Bliesner et al., 2014; Voigt et al., 2015).

80 Transient simulations using comprehensive CGCMs are hugely affected by model
81 speed restrictions and often 'acceleration techniques' are adopted for multi-millennial
82 (or longer) palaeoclimate simulations (e.g. Lorenz and Lohmann, 2004; Varma et al.,
83 2012; Smith and Gregory 2012; Bakker et al., 2014; Kwiatkowski et al., 2015).
84 Specifically, acceleration of slowly varying orbital variations has been employed.
85 Earlier studies have already been conducted to test the undesired effects of
86 acceleration techniques in the boundary conditions on climate simulations, but have
87 used EMICs only (Lunt et al., 2006; Timm and Timmermann, 2007). In this study, we
88 employ a comprehensive CGCM to examine the evolution of basic climate parameters
89 under temporally varying orbital forcing for the present and last interglacial periods,
90 using transient simulations with and without acceleration of the external forcing. The
91 basic assumption for the application of this acceleration technique is that orbital
92 forcing operates on much longer timescales than those inherent in the atmosphere and
93 upper ocean layers (Lorenz and Lohmann, 2004).

94

95 **2 Methods**

96 Multi-millennial transient simulations were performed using the comprehensive
97 global CGCM CCSM3 (Community Climate System Model version 3). NCAR's
98 (National Center for Atmospheric Research) CCSM3 is a state-of-the-art fully
99 coupled model, composed of four separate components representing atmosphere,
100 ocean, land and sea ice (Collins et al., 2006). Here, we employ the low-resolution
101 version described in detail by Yeager et al. (2006). In this version the resolution of the

atmospheric component is given by T31 (3.75° transform grid), with 26 layers in the vertical, while the ocean has a nominal resolution of 3° with refined meridional resolution (0.9°) around the equator and a vertical resolution of 25 levels. The sea-ice component shares the same horizontal grid with the ocean model.

The time periods of interest in this study are the present interglacial (PIG) (11.7 – 0 kyr BP, kiloyears before present) and the last interglacial (LIG) (ca. 130 – 115 kyr BP). On these multi-millennial time-scales, it is the periodic changes in the Earth's orbital parameters that cause the modifications of seasonal and latitudinal distribution of insolation at the top of the atmosphere (Berger, 1978), acting as the prime forcing of long-term interglacial climate change.

The climatic precession parameter increased during both the PIG and the LIG (from ~127 kyr BP onward; Fig. 1). As a result, there was a weakening of the seasonal insolation amplitude in the Northern Hemisphere resulting in a decrease in the boreal summer insolation (Berger, 1978). For the LIG, the variability in climatic precession was more pronounced compared to the PIG due to a larger orbital eccentricity. Hence, the effect of orbital forcing on climate is expected to be stronger (Fig. 1b). Additionally, the obliquity decreased by ~0.5° to 1° over the interglacials resulting in a decrease of insolation in the summer hemisphere as well as total annual insolation at southern and northern high latitudes (Loutre et al., 2004). We note that the total annual insolation at a given latitude does not depend on precession.

Accelerated and non-accelerated transient simulations covering the two interglacials (9 to 2 kyr BP for the PIG and 130 to 120 kyr BP for the LIG) were carried out under varying orbital forcing only. The experimental set-ups for the accelerated PIG and LIG simulations are described in Varma et al. (2012) and Bakker et al. (2013), respectively. In both simulations, the orbital forcing is accelerated by a factor 10 (the orbital parameters were changed every 10 model years, but with 100 year forward time steps). Therefore, climate trends over 7,000 (PIG experiment) and 10,000 years (LIG experiment) imposed by the external orbitally driven insolation changes, are represented in the accelerated experiments by only 700 and 1000 simulation years, respectively.

Throughout all runs pre-industrial aerosol and ozone distributions as well as modern ice sheet configurations were prescribed. The greenhouse gas concentrations in the LIG runs take the mean value for the period 130 – 120 kyr BP (i.e. CO_2 = 272 ppm, CH_4 = 622 ppb and N_2O = 259 ppb; Loulergue et al., 2008, Lüthi et al., 2008, Spahni

136   et al., 2005). Throughout the PIG experiments, greenhouse gas concentrations were

137   kept constant at pre-industrial values (CO_2 = 280 ppm, CH_4 = 760 ppb and N_2O = 270

138   ppb).

139   Initialization of the accelerated and the non-accelerated PIG transient simulation was

140   identical: from a pre-industrial quasi-equilibrium simulation (Merkel et al., 2010), the

141   model was integrated for 400 years with fixed boundary conditions representing 9 kyr

142   BP orbital forcing and pre-industrial atmospheric composition. Both transient

143   simulations started from the final state of this time slice run. The LIG transient

144   simulations were initialized as follows: the final state of the 9 kyr BP simulation was

145   used to initialize a 130 kyr BP time slice run. This 130 kyr BP run was integrated for

146   another 400 years with fixed boundary conditions representing 130 kyr BP orbital

147   forcing and atmospheric composition as in the transient LIG runs (see above), which

148   were then started from the final 130 kyr BP state. We note that 400 years of spin-up

149   were not enough to bring the deep ocean to a perfectly steady state.

150   Forcing of accelerated and non-accelerated transient runs differs only in the rate of

151   change of orbital parameters (similar to the accelerated runs, orbital parameters were

152   updated every 10 integration years also in the non-accelerated simulations). This

153   approach allows the identification of acceleration effects by direct comparison of the

154   accelerated and non-accelerated runs.

155   For the analyses of the model results decadal means (referring to model years) have

156   been used from all the transient simulations. The main focus of our analysis is on the

157   basic climate fields surface temperature and precipitation. In addition, we analyze the

158   evolution of global deep ocean temperature and sea ice in order to elucidate high-

159   latitude features we observe in the sea-surface temperature fields, as well as low-level

160   (850 hPa) zonal wind in order to assess the potential impact of sea-surface

161   temperature biases on atmosphere dynamics.

162   To investigate and visualize spatio-temporal climate variability we employ Hovmöller

163   diagrams and Empirical Orthogonal Function (EOF) analysis. The EOFs (or principal

164   components) were found by computing the eigenvalues and eigenvectors of the

165   covariance matrix of a climatic field (e.g. von Storch and Zwiers, 2004). The derived

166   eigenvalues provide a measure of the percent variance explained by each mode (the

167   first or leading mode provides the highest variance in the analyzed field). The time

168   series of each mode were obtained by projecting the derived eigenvectors onto the

169   spatially weighted anomalies.

3 Results

Fig. 2 shows the simulated evolution of annual-mean global ocean temperatures at depths of 4 m (surface), 437 m and 1884 m for both interglacials. The surface temperature for the PIG shows considerable differences between the accelerated and non-accelerated runs, especially during the early-to-mid PIG (Fig. 2a). While there is a pronounced decreasing trend in surface temperature for the non-accelerated run during the time period 9 – 7 kyr BP, this is not captured in the accelerated PIG run. The 437 m temperature evolution for the PIG shows reasonably similar trends in both accelerated and non-accelerated simulations (Fig. 2c). However, at deeper levels (1884 m) there is an overall significant difference quantitatively between the accelerated and non-accelerated PIG runs (Fig. 2e). While there is a drop of ~0.4°C in the deep-ocean temperature in the non-accelerated simulation during the early PIG, the accelerated run is underestimating this decreasing trend and shows a strongly delayed and much more stable response.

For the LIG, the temperatures at the surface and at 437 m depths show overall similar responses in both accelerated and non-accelerated runs, though there are some differences during the late LIG (Figs. 2b and 2d). However, like in the PIG, the response of 1884 m temperature is quite contrasting in the LIG as well (Fig. 2f). The deep-ocean temperature is showing a decreasing trend during the early-to-mid LIG and then an increasing trend for the mid-to-late LIG in the non-accelerated run (Fig. 2f). Not only is this trend variability missing in the accelerated run, also the general temperature evolution during the LIG is quantitatively underestimated. While the change in 1884 m temperature during the LIG is ~0.3°C in the non-accelerated simulation, it is just about 0.06°C in the accelerated run (Fig. 2f).

Fig. 3 represents the evolution of zonally averaged surface temperature for both interglacials. For the PIG, in response to orbital forcing, it is the high latitudes that show a robust cooling response, in both accelerated and non-accelerated simulations (Figs. 3a, b). It also shows a warming of the tropics during the mid-to-late PIG in both the simulations. The anomaly between simulations with and without orbital acceleration (Fig. 3c) clearly shows that there are evident disparities in the high latitudes especially during the early-to-mid PIG, when the southern high-latitude cooling in the accelerated simulation lags (and underestimates) the cooling in the non-accelerated run. For the LIG, the northern high latitudes tend to show a slight warming between ~130 – 125 kyr BP and then an intense cooling trend afterwards in

both non-accelerated and accelerated simulations (Fig. 3d,e). The southern high latitudes show a cooling trend during the early LIG in the non-accelerated run, followed by a warming trend during the late LIG. By contrast, a steady cooling trend in the southern high latitudes is simulated in the accelerated run. The low latitudes show strongest warming from mid-to-late LIG in both the simulations.

Fig. 4 displays the evolution of zonally averaged zonal wind at 850 hPa for both interglacials. A pronounced strengthening of the zonal wind circulation in the southern high mid-latitudes (ca. 50-60°S) is simulated in the non-accelerated PIG run (Fig. 4a). There is a similar trend observed in the accelerated simulation as well but less intense and delayed in time compared to its non-accelerated counterpart (Fig. 4b). This wind intensification at the southern flank of the Southern Westerly Wind (SWW) belt is accompanied by a decrease of zonal wind speed at the northern flank of the SWW region (ca. 30-40°S), which can be depicted as a general poleward shift of the SWW during the PIG under orbital forcing as described in an earlier study (Varma et al., 2012). Similarly, during the LIG a poleward shift of the SWW under orbital forcing is observed in both non-accelerated and accelerated simulations as well, albeit more robust compared to the PIG response (Fig. 4d,e). Meanwhile, the Northern Hemisphere westerly winds appear to shift northward (weakening of the winds around 30°N and strengthening around 50-60°N), the northeast trade winds (south of ca. 20°N in the Northern Hemisphere) become stronger and the southeast trade winds (north of ca. 20°S) weaker during all the interglacial simulations. The changing trade winds indicate a southward shift of the global mean intertropical convergence zone throughout the PIG and the LIG (cf. Schneider et al., 2014).

Fig. 5 shows the evolution of global surface temperature during the PIG, for both non-accelerated and accelerated runs decomposed into EOFs. The first EOF shows a general cooling trend of the high latitudes in both hemispheres in both non-accelerated and accelerated simulations. The cooling is more pronounced in the northern high latitudes in response to the changes in insolation. Maximum cooling is observed around Baffin Bay extending up to the Labrador Sea in both the simulations (Figs. 5a,e). Sea-ice effects play a role here in amplifying the climatic response to the orbital forcing, as evident from the first EOF of sea ice concentration (Fig. 6). Another feature observed in both simulations is the general warming trend in the tropics, especially over the Sahel and Indian regions, which is mainly attributed to climate feedbacks associated with orbital-induced weakening of the monsoons (e.g.

238   Bakker et al., 2013). The second EOF shows strong variability in the Nordic Seas,
239   associated with shifts in the sea-ice margin in both non-accelerated and accelerated
240   simulations (Fig. 5c,g; Fig. 6c,g).
241   Even though the general spatial patterns of the two leading EOFs are similar between
242   the accelerated and the non-accelerated simulation, some differences in the EOF maps
243   are evident especially in the northern North Atlantic and Nordic Seas as well as in the
244   Southern Ocean. Moreover, the first principal component exhibits a rather linear trend
245   throughout the Holocene in the accelerated simulation (Fig. 5f), whereas an increased
246   rate of change can be observed during the early Holocene in the first principal
247   component of the non-accelerated run (Fig. 5b).
248   The spatio-temporal evolution of global surface temperature during the LIG is
249   represented in Fig. 7 by means of the two leading EOFs. The observed high latitude
250   cooling in the Northern Hemisphere is more pronounced in the LIG compared to the
251   PIG in line with larger insolation changes. Similar is the case with the tropics where
252   the warming is more pronounced compared to the PIG. These patterns are very similar
253   in the first EOFs of both non-accelerated and accelerated simulations (Fig. 7a,e). The
254   second EOFs reflect strong variability in the northern North Atlantic. As for PIG, sea
255   ice variations are closely related to high-latitude surface temperature variability (Fig.
256   8). In general, both non-accelerated and accelerated simulations share similar
257   response patterns in the second EOF (Fig. 7c,g). However, both leading EOFs reveal
258   pronounced differences between non-accelerated and accelerated runs in the Southern
259   Ocean sector, similar to what has been found for the PIG simulations.
260   Fig. 9 shows the leading two EOFs for global precipitation during the PIG for both
261   non-accelerated and accelerated simulations. The first EOF of both simulations
262   reveals a general weakening of the North African and Indian monsoon systems along
263   with a strengthening of Southern Hemisphere monsoons (Fig. 9a,e). The second EOF
264   does not contain a long-term (orbitally driven) trend, but rather shows a pattern of
265   (multi-)decadal tropical precipitation variability. This EOF is not significantly
266   affected by the acceleration either.
267   Fig. 10 depicts the evolution of global precipitation during the LIG in both non-
268   accelerated and accelerated simulations. Similar to the PIG, there is a decreasing trend
269   in North African and Indian monsoonal rainfall along with increasing precipitation
270   over South America, Southern Africa and Australia (Fig. 10a,e), albeit more
271   pronounced than during the PIG. The second EOF contains a long-term (orbitally

272 forced) signal, but explains only ca. 8% of the total variance in both the accelerated

273 and the non-accelerated run. Again, orbital acceleration hardly affects the

274 precipitation EOFs.

275 Fig. 11 displays the temporal evolution of the Atlantic Meridional Overturning

276 Circulation (AMOC) during both interglacials. During the PIG, the AMOC generally

277 shows a decreasing trend, whereas an increasing trend is simulated for the LIG. The

278 long-term LIG AMOC trend is hardly affected by the acceleration. Overall, the

279 AMOC shows relatively small changes in all experiments. Therefore, shifts in rainfall

280 in tropical/monsoonal regions and global surface temperature patterns are (to first

281 order) free from internal AMOC-related changes.

282

283 **4 Discussion**

284 Our analysis of time series and EOF patterns has shown that the interglacial evolution

285 of simulated surface climate variables (temperature, precipitation, wind) is hardly

286 affected by the application of an orbital acceleration factor 10 in low latitudes,

287 whereas noticeable differences may arise in extratropical regions. The regional biases

288 resulted in acceleration-induced global mean sea-surface temperature biases of about

289 0.05-0.1°C during the early-to-mid PIG and the late LIG in our simulations (Fig. 2).

290 To further specify the regions were acceleration-induced biases are greatest we

291 calculated global maps of root-mean-square differences between the accelerated and

292 the non-accelerated runs over the low-pass filtered surface temperature time series for

293 the PIG and the LIG (Fig. 12). For the PIG, the largest acceleration-induced biases are

294 found in the Southern Ocean and the Nordic Seas, i.e. regions where the surface

295 climate has a direct connection to the deep ocean (upwelling of deep water in the

296 Southern Ocean, deep convection regions in the northern and southern high latitudes).

297 Acceleration-induced biases in these high-latitude regions are further amplified by

298 sea-ice feedbacks (cf. Timmermann et al., 2014). A qualitatively similar result is

299 found for the LIG (Fig. 12b), however, the Northern Hemisphere maximum has

300 shifted to the northern North Atlantic. This is because deep convection disappears

301 from the Nordic Seas in the LIG simulations associated with excessive sea ice.

302 Instead, deep convection and hence deep-water formation mostly takes place south of

303 the Denmark Strait in both the accelerated and the non-accelerated LIG runs (not

304 shown). In general, root-mean-square deviations are larger during the PIG than during

305 the LIG; in other words, PIG climate simulations appear more susceptible to

acceleration-induced biases than LIG simulations. We hypothesize that the stronger orbital forcing during the LIG compared to the PIG (Fig. 1) puts a stronger constraint on the evolution of surface temperature such that biases associated with heat exchange with the deep ocean have a weaker impact. The stronger insolation forcing of the LIG compared to the PIG is also evident in the temporal evolution of global precipitation patterns as derived from the EOF analysis: About 65% of the precipitation variance during the LIG is related to orbital forcing (and spreading over the leading two EOFs), whereas only ca. 31% of the precipitation variance is associated with orbital forcing during the PIG (and only contained in the first EOF). We note that orbital variations do not show up in higher modes either.

In accelerated simulations, temperature changes in the slowly adjusting deep ocean with its huge heat reservoir are damped and delayed relative to their non-accelerated counterparts. This global-scale delayed response affects sea-surface temperatures at high latitudes. A deep-ocean cooling trend in the non-accelerated PIG run is not equally simulated in the accelerated run (Fig. 2e). As a result, the deep ocean has a warm bias throughout the Holocene in the accelerated simulation, which has a counterpart at the surface in high latitudes (Figs. 2a and 3c). Similarly, a cold deep-ocean bias during the late LIG in the accelerated run (Fig. 2f) has a surface counterpart at high southern latitudes (Figs. 2b, 3f). Previous studies conducted to test the effects of acceleration techniques in the boundary conditions on climate simulations using EMICs came to similar conclusions regarding sea-surface temperature biases at high latitudes (Lunt et al., 2006; Timm and Timmermann, 2007). In these regions, inappropriate deep-ocean initial conditions may severely compromise accelerated runs, strongly determining the climate trajectories. This becomes evident from the fact that the deep ocean has an adjustment timescale in the order of 1000 years or longer, which implies that the entire accelerated integration of an interglacial (using an acceleration factor 10) is influenced by the initialization. In particular, we suggest that a considerable portion of the long-term deep-ocean cooling/warming trend in the accelerated PIG/LIG run (Fig. 2e,f) may be related to an adjustment to an imbalance between the initial state and the applied boundary conditions at the beginning of the transient simulation.

Biased sea-surface temperatures may affect the dynamics of the overlying atmosphere. In our simulations, such an effect was particularly pronounced in the PIG runs for the SWW, which are influenced by Southern Ocean temperatures, but also for

340 the Northern Hemisphere westerly wind belt. In low latitudes, where the ocean is well

341 stratified and does not exchange with the deep ocean, the effect of orbital acceleration

342 on surface winds and (monsoonal) rainfall is negligible (cf. Govin et al., 2014).

343 Our transient interglacial simulations were forced by changes in orbital parameters

344 and associated insolation only. Other forcing factors, in particular atmospheric

345 greenhouse gas concentrations were kept constant. However, there is no reason to

346 assume that acceleration would affect the simulated climate response to slowly

347 varying greenhouse gas (longwave) radiative forcing in a much different way than

348 varying orbital (shortwave) radiative forcing. Hence, our conclusions for the

349 acceleration of orbital forcing should also hold true for greenhouse gas forcing.

350 Acceleration techniques have been invented for the study of long-term (e.g. orbitally

351 driven) climate variations. It is needless to mention that centennial-to-millennial scale

352 variability cannot be studied in our accelerated PIG and LIG runs, which were only

353 integrated for 700 and 1000 model years, respectively. By contrast, interannual-to-

354 decadal variability can, in principle, be studied in the accelerated runs. For this

355 purpose, the modelled time series should be analyzed on the model time-axis. For

356 example, if one would like to examine interannual variability during the mid-

357 Holocene (say, 7-6 kyr BP), a 10-times accelerated PIG run provides a 100-year time

358 series to analyze high-frequency climate variations. The next 100 years of model

359 output could be used to study the interannual variability for 6-5 kyr BP, and so on. In

360 so doing, the temporal evolution of interannual variability through the Holocene could

361 be evaluated by means of an accelerated simulation.

362 In summary, it can be stated that results from accelerated interglacial CGCM

363 simulations are meaningful when low-latitude climate is considered. In these regions,

364 the acceleration technique does neither hamper model intercomparison nor model-

365 data comparison studies such as, e.g., Bakker et al. (2013, 2014) and Kwiatkowski et

366 al. (2015), in which accelerated simulations have been employed. In high latitudes,

367 however, the use of acceleration techniques can substantially affect the surface

368 temperature such that acceleration should be avoided in studies of extratropical

369 climate change.

370

371 **5 Conclusions**

372 Transient simulations from a fully coupled comprehensive climate model have been

373 analysed to study the effects of orbital acceleration on the present and last interglacial

374 climates. To this end, simulations were carried out both with and without orbital

375 acceleration. Comparison of the results from these simulations shows that in low

376 latitudes the simulation of long-term variations in interglacial surface climate is not

377 significantly affected by the use of the acceleration technique (with an acceleration

378 factor 10) and hence model-data comparison of surface variables is therefore not

379 hampered. However, due to the long adjustment time of the deep ocean with its huge

380 heat reservoir, major repercussions of the orbital forcing are obvious below the

381 thermocline. As a result, acceleration-induced biases in sea-surface temperature

382 evolution arise in high-latitude regions where the surface climate has a direct

383 connection to the deep ocean (upwelling of deep water in the Southern Ocean, deep

384 convection regions at high latitudes). Sea-ice feedbacks amplify the temperature

385 biases. In these regions, the climate trajectory can be crucially determined by the

386 deep-ocean initialization of the accelerated transient simulation. It was further found

387 that the temporal evolution of the southern and northern westerlies could be affected

388 by sea-surface temperature biases. As such, the acceleration technique may

389 compromise transient climate simulations over large regions in the extratropics, such

390 that special care has to be taken or acceleration should be avoided.

391

404

405

406

407

12

408 **References**

409 Bakker, P., Masson-Delmotte, V., Martrat, B., Charbit, S., Renssen, H., Gröger, M.,

410 Krebs-Kanzow, U., Lohman, G., Lunt, D.J., Pfeiffer, M., Phipps, S.J., Prange, M.,

411 Ritz, S.P., Schulz, M., Stenni, B., Stone, E.J., Varma, V.: Temperature trends during

412 the Present and Last Interglacial periods – a multi-model-data comparison,

413 Quaternary Science Reviews, Volume 99, pp. 224-243, doi:

414 http://dx.doi.org/10.1016/j.quascirev.2014.06.031, 2014.

415 Bakker, P., Stone, E. J., Charbit, S., Gröger, M., Krebs-Kanzow, U., Ritz, S. P.,

416 Varma, V., Khon, V., Lunt, D. J., Mikolajewicz, U., Prange, M., Renssen, H.,

417 Schneider, B., and Schulz, M.: Last interglacial temperature evolution – a model

418 inter-comparison, Climate of the Past, 9, pp. 605-619, doi: 10.5194/cp-9-605-2013,

419 2013.

420 Berger, A. L.: Long-term variations of daily insolation and Quaternary climatic

421 changes, J. Atmos. Sci., 35, 2362–2367, doi:10.1175/1520-0469(1978)0352.0.CO;2,

422 1978.

423 Braconnot, P., Otto-Bliesner, B., Harrison, S., Joussaume, S., Peterchmitt, J.-Y., Abe-

424 Ouchi, A., Crucifix, M., Driesschaert, E., Fichefet, Th., Hewitt, C. D., Kageyama, M.,

425 Kitoh, A., Laîné, A., Loutre, M.-F., Marti, O., Merkel, U., Ramstein, G., Valdes, P.,

426 Weber, S. L., Yu, Y., and Zhao, Y.: Results of PMIP2 coupled simulations of the

427 Mid-Holocene and Last Glacial Maximum – Part 1: experiments and large-scale

428 features, Clim. Past, 3, 261-277, doi:10.5194/cp-3-261-2007, 2007.

429 Claussen, M., Mysak, L. A., Weaver, A. J., Crucifix, M., Fichefet, T., Loutre, M. –F.,

430 Weber, S. L., Alcamo, J., Alexeev, V. A., Berger, A., Calov, R., Ganopolski, A.,

431 Goosse, H., Lohmann, G., Lunkeit, F., Mokhov, I. I., Petoukhov, V., Stone, P., and

432 Wang, Z.: Earth system models of intermediate complexity: closing the gap in the

433 spectrum of climate system models, Clim. Dyn., 18, 579–586, 2002.

434 Collins, W. D., Bitz, C. M., Blackmon, M. L., Bonan, G. B., Bretherton, C. S.,

435 Carton, J. A., Chang, P., Doney, S. C., Hack, J. J., Henderson, T. B., Kiehl, J. T.,

436 Large, W. G., McKenna, D. S., Santer, B. D., and Smith, R. D.: The Community

437 Climate System Model Version 3 (CCSM3), J. Climate, 19, 2122–2143,

438 doi:10.1175/JCLI3761.1, 2006.

439 Govin, A., V. Varma, and M. Prange, 2014: Astronomically forced variations in

440 western African rainfall (21°N-20°S) during the Last Interglacial period. Geophysical

441 Research Letters, 41, 2117-2125, doi:10.1002/2013GL058999.

442 Kwiatkowski, C., Prange, M., Varma, V., Steinke, S., Hebbeln, D., and Mohtadi, M.:
443 Holocene variations of thermocline conditions in the eastern tropical Indian
444 Ocean, Quaternary Sci. Rev., 114, 33-42, doi:10.1016/j.quascirev.2015.01.028, 2015.

445 Liu, Z., Zhu, J., Rosenthal, Y., Zhang, X., Otto-Bliesner, B. L., Timmermann, A.,
446 Smith, R. S., Lohmann, G., Zheng, W., and Elison Timm, O.: The Holocene
447 temperature conundrum, Proc. Natl. Acad. Sci., 111(34), E3501–E3505,
448 doi:10.1073/pnas.1407229111, 2014.

449 Lorenz, S. J. and Lohmann, G.: Acceleration technique for Milankovitch type forcing
450 in a coupled atmosphere-ocean circulation model: method and application for the
451 Holocene, Clim. Dyn., 23, 727–743, 2004.

452 Loulergue, L., Schilt, A., Spahni, R., Masson-Delmotte, V., Blunier, T., Lemieux, B.,
453 Barnola, J. −M., Raynaud, D., Stocker, T. F., and Chappellaz, J.: Orbital and
454 millennial-scale features of atmospheric CH4 over the past 800,000 years. Nature,
455 Vol. 453, 383-386, doi:10.1038/nature06950, 2008.

456 Loutre, M.-F. , Paillard, D. , Vimeux, F. & Cortijo, E. Does mean annual insolation
457 have the potential to change the climate? Earth Planet. Sci. Lett. 221, 1–14 (2004).

458 Lunt, D. J., Abe-Ouchi, A., Bakker, P., Berger, A., Braconnot, P., Charbit, S.,
459 Fischer, N.,   Herold, N.,   Jungclaus, J. H.,   Khon, V. C.,   Krebs-Kanzow, U.,
460 Langebroek, P. M., Lohmann, G., Nisancioglu, K. H., Otto-Bliesner, B. L., Park, W.,
461 Pfeiffer, M., Phipps, S. J., Prange, M., Rachmayani, R., Renssen, H., Rosenbloom, N.,
462 Schneider, B., Stone, E. J., Takahashi, K., Wei, W., Yin, Q., and Zhang, Z. S.: A
463 multi-model assessment of last interglacial temperatures, Clim. Past, 9, 699-717,
464 doi:10.5194/cp-9-699-2013, 2013.

465 Lunt, D. J.,   Williamson, M. S.,   Valdes, P. J.,   Lenton, T. M.,   and   Marsh, R.:
466 Comparing transient, accelerated, and equilibrium simulations of the last 30 000 years
467 with the GENIE-1 model, Clim. Past, 2, 221-235, doi:10.5194/cp-2-221-2006, 2006.

468 Lüthi, D., Le Floch, M., Bereiter, B., Blunier, T., Barnola, J. −M., Siegenthaler, U.,
469 Raynaud, D., Jouzel, J., Fischer, H., and Kawamura, K., and Stocker, T. F.: High-
470 resolution carbon dioxide concentration record 650,000-800,000 years before present,
471 Nature, 453, 379-382, doi:10.1038/nature06949, 2008.

472 Merkel, U., Prange, M., and Schulz, M.: ENSO variability and teleconnections during
473 glacial   climates,   Quaternary   Sci.   Rev.,   29,   86–100,
474 doi:10.1016/j.quascirev.2009.11.006, 2010.

475 Milker, Y., Rachmayani, R., Weinkauf, M. F. G., Prange, M., Raitzsch, M., Schulz,
476 M., and Kucera, M.: Global and regional sea surface temperature trends during
477 Marine Isotope Stage 11. Clim. Past, 9, 2231-2252, doi:10.5194/cp-9-2231-2013,
478 2013.

479 Otto-Bliesner, B.L., Russell, J. M., Clark, P. U., Liu, Z., Overpeck, J. T., Konecky, B.,
480 deMenocal, P., Nicholson, S. E., He, F., and Lu, Z.: Coherent changes of southeastern
481 equatorial and northern African rainfall during the last deglaciation, Science, 346,
482 1223-1227, 2014.

483 Rachmayani, R., M. Prange, and M. Schulz, 2016: Intra-interglacial climate
484 variability: model simulations of Marine Isotope Stages 1, 5, 11, 13, and 15. Climate
485 of the Past, 12, 677-695, doi:10.5194/cp-12-677-2016.

486 Schneider, T., Bischoff, T., and Haug, G. H.: Migrations and dynamics of the
487 intertropical convergence zone, Nature, 513, 45-53, 2014.

488 Smith, R. and Gregory, J.: The last glacial cycle: transient simulations with an
489 AOGCM, Clim. Dynam., 38, 1545–1559, doi:10.1007/s00382-011-1283-y, 2012.

490 Spahni, R., Chappellaz, J., Stocker, T. F., Loulergue, L., Hausammann, G.,
491 Kawamura, K., Fluckiger, J., Schwander, J., Raynaud, D., Masson-Delmotte, V., and
492 Jouzel, J.: Atmospheric Methane and Nitrous Oxide of the Late Pleistocene from
493 Antarctic Ice Cores, Science, 310, 1317–1321, 2005.

494 Timm, O., and A. Timmermann: Simulation of the last 21,000 years using accelerated
495 transient boundary conditions. J. Climate, 20, 4377–4401,IPRC-439, 2007.

496 Timmermann, A., T. Friedrich, O. Elison Timm, M. O. Chikamoto, A. Abe-Ouchi,
497 and A. Ganopolski (2014), Modeling Obliquity and CO2 Effects on Southern
498 Hemisphere Climate during the Past 408 ka, J. Clim., 27(5), 1863–1875,
499 doi:10.1175/JCLI-D-13-00311.1.

500 Varma, V., Prange, M., Merkel, U., Kleinen, T., Lohmann, G., Pfeiffer, M.,
501 Renssen, H., Wagner, A., Wagner, S., and Schulz, M.: Holocene evolution of the
502 Southern Hemisphere westerly winds in transient simulations with global climate
503 models, Clim. Past, 8, 391-402, doi:10.5194/cp-8-391-2012, 2012.

504 Voigt, I., Chiessi, C. M., Prange, M., Mulitza, S., Groeneveld, J., Varma, V., and
505 Henrich, R.: Holocene shifts of the southern westerlies across the South Atlantic,
506 Paleoceanography, 30, doi:10.1002/2014PA002677, 2015.

507 von Storch, H., Zwiers, F.W.: Statistical Analysis in Climate Research. Cambridge
508 University Press, 2004.

509   Yeager, S. G., Shields, C. A., Larger, W. G., and Hack, J. J.: The low-resolution

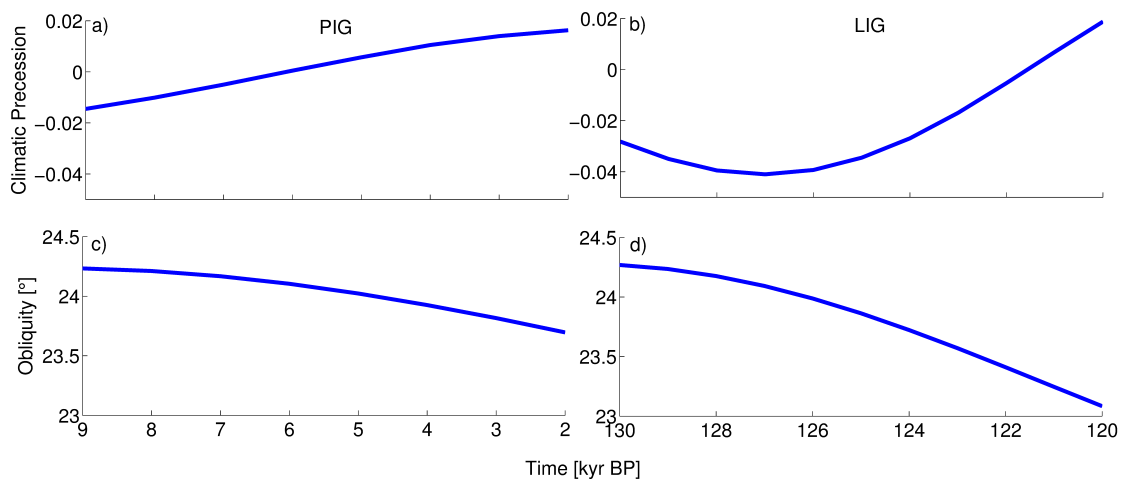510   CCSM3, J. Climate, 19, 2545–2566, doi:10.1175/JCLI3744.1, 2006.

511

512

513

514

515

516

517

518

519

520

521

522

523

524

525

526

527

528

529

530

531

532

533

534

535

536

537

538

539

540

541

542

Figure captions

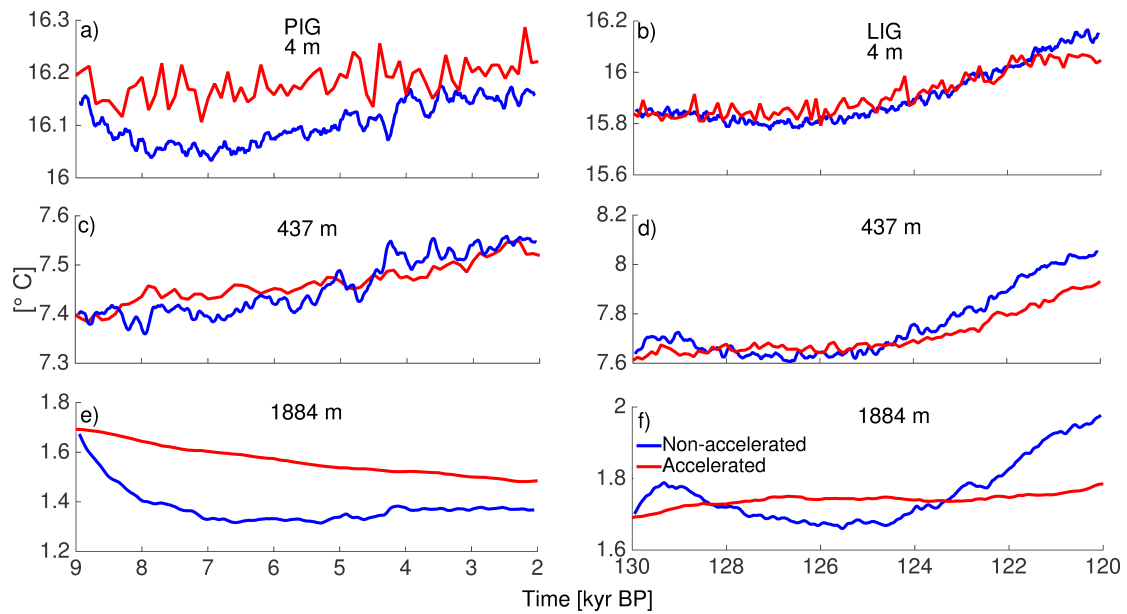Fig. 1 Orbital parameters in the transient experiments for the PIG (a, c) and the LIG (b, d) (Berger, 1978).

Fig. 2 Evolution of global mean potential ocean temperature at various depths for the PIG (a, c, e) and the LIG (b, d, f). Blue lines represent the non-accelerated simulations and red lines represent the accelerated simulations. All plots were created using the decadal mean values (referring to model years). In addition, a 10-point running average was applied to the decadal mean values of the non-accelerated simulations. Time series of the accelerated runs were mapped onto orbital time-axes, such that 10 model years represent 100 orbital years, and hence appear stretched in time.

18
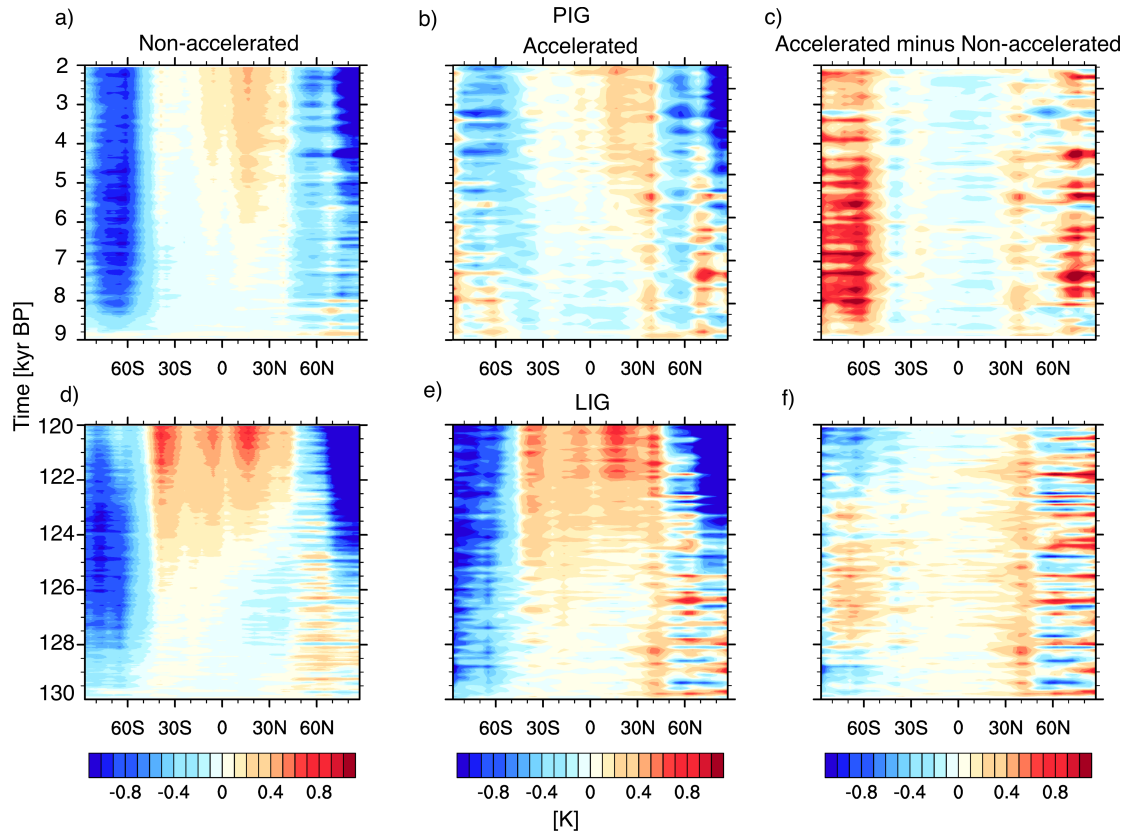
Figure 3. Evolution of zonally averaged surface temperature anomalies (including ocean and land) during interglacials for both non-accelerated (a, d) and accelerated (b, e) simulations. Shown are anomalies relative to 9 kyr BP (PIG) and 130 kyr BP (LIG). Differences in the temperature evolution between accelerated and non-accelerated simulations are also displayed (c, f). All plots were created using the decadal mean values (referring to model years). In addition, a 10-point running average was applied to the decadal mean values of the non-accelerated simulations.
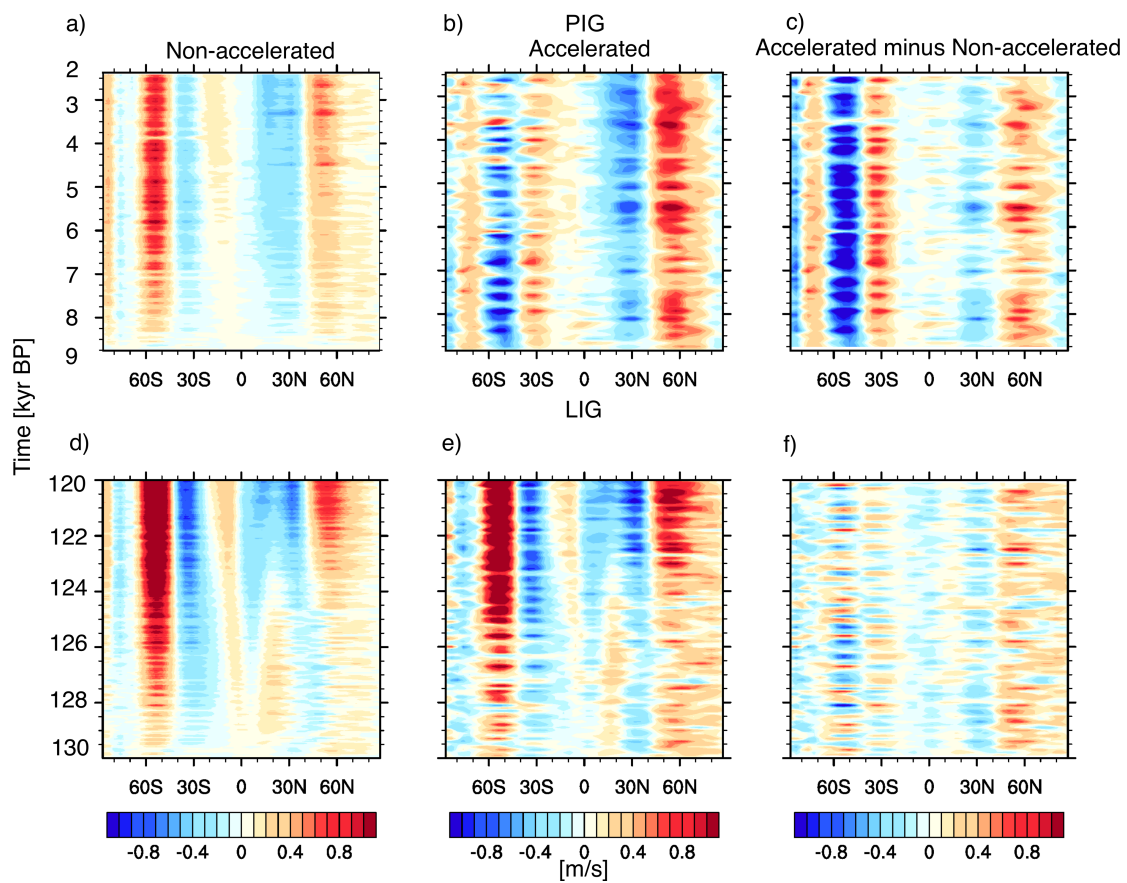
Figure 4. Same as Fig. 3 but for 850 hPa zonal wind.
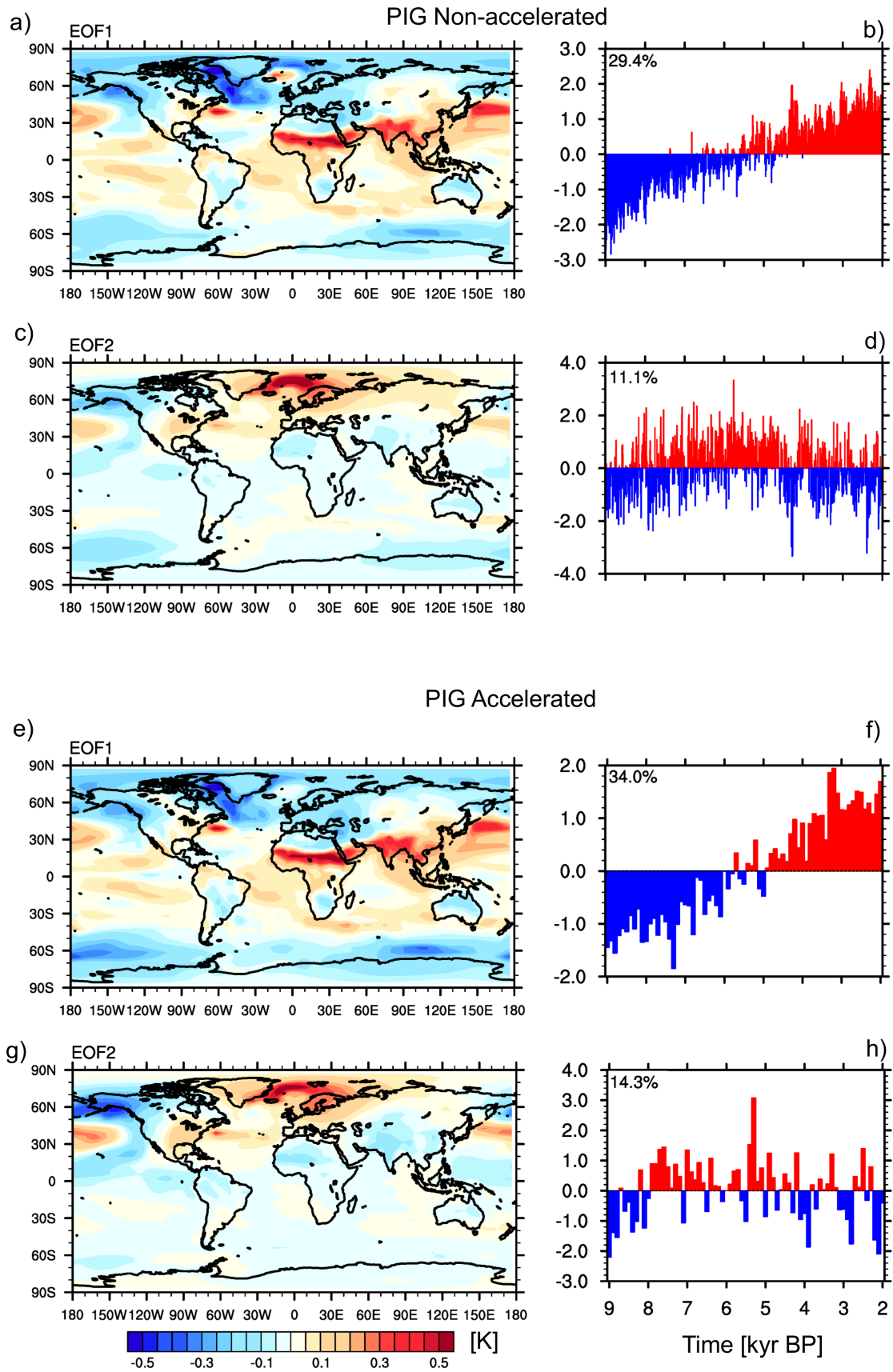
Figure 5. Leading two EOFs of annual-mean surface temperature calculated from the non-accelerated (a-d) and accelerated (e-h) PIG simulations. Explained variances of

594   each EOF are specified in the principal component (time series) plots (b, d, f, h). All

595   EOF analyses were performed on serial decadal mean values (referring to model

596   years) from the transient simulations. Principal components are standardized and the

597   EOF maps (a, c, e, g) were obtained by regressing the surface temperature data onto

598   the corresponding standardized principal component time series.

599

600

601
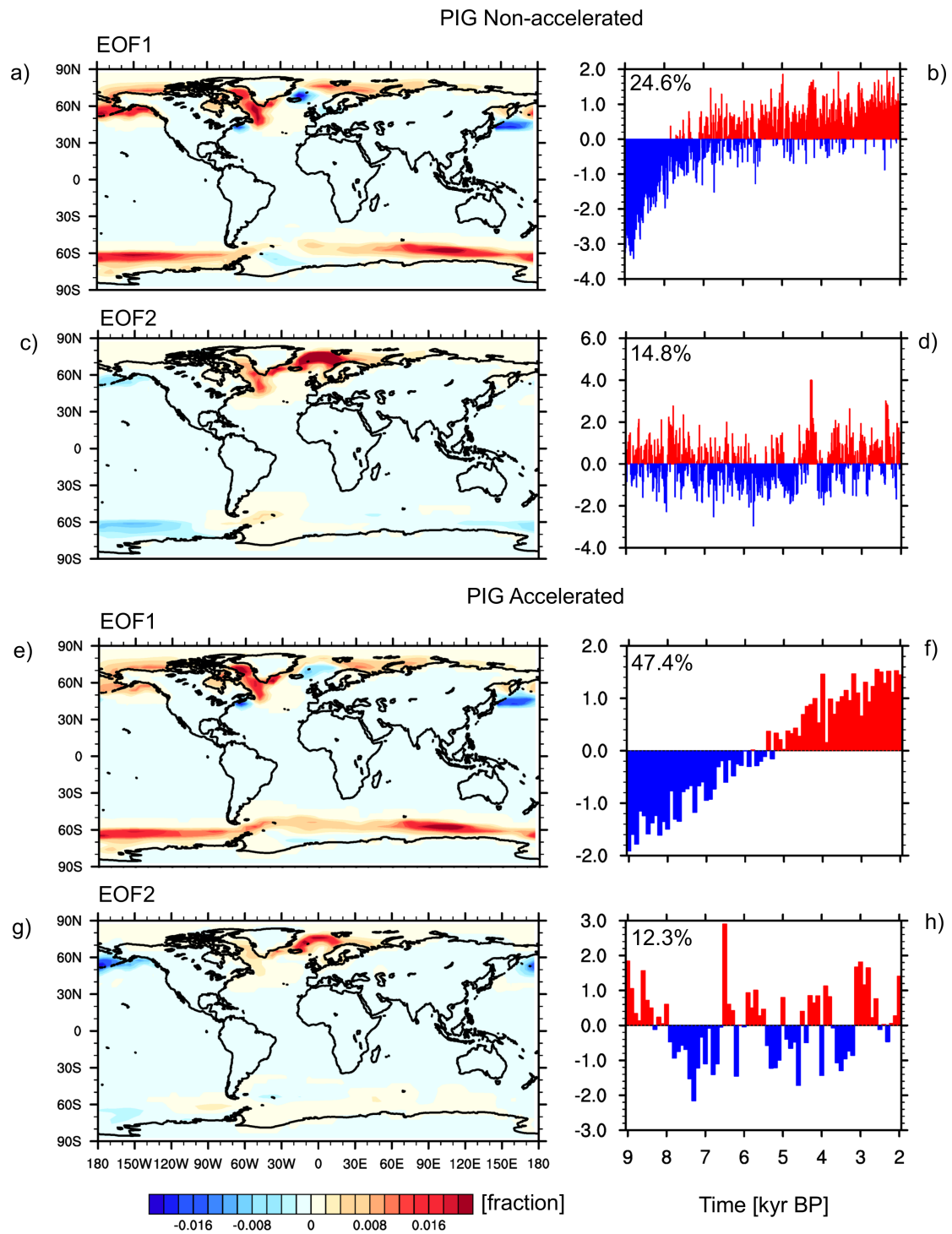
Figure 6. Same as Fig. 5 but for PIG sea-ice concentration.
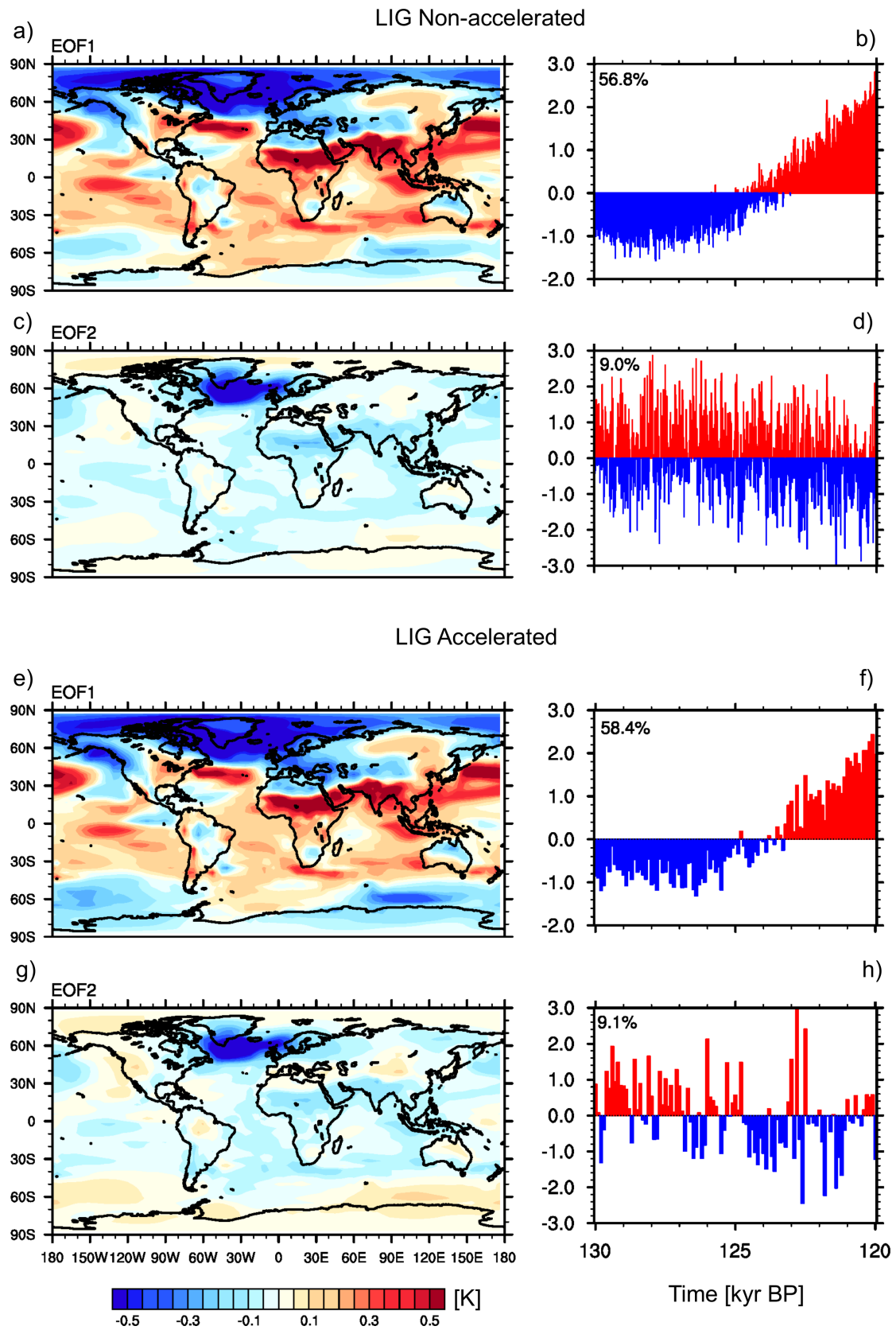
Figure 7. Same as Fig. 5 but for LIG surface temperature.
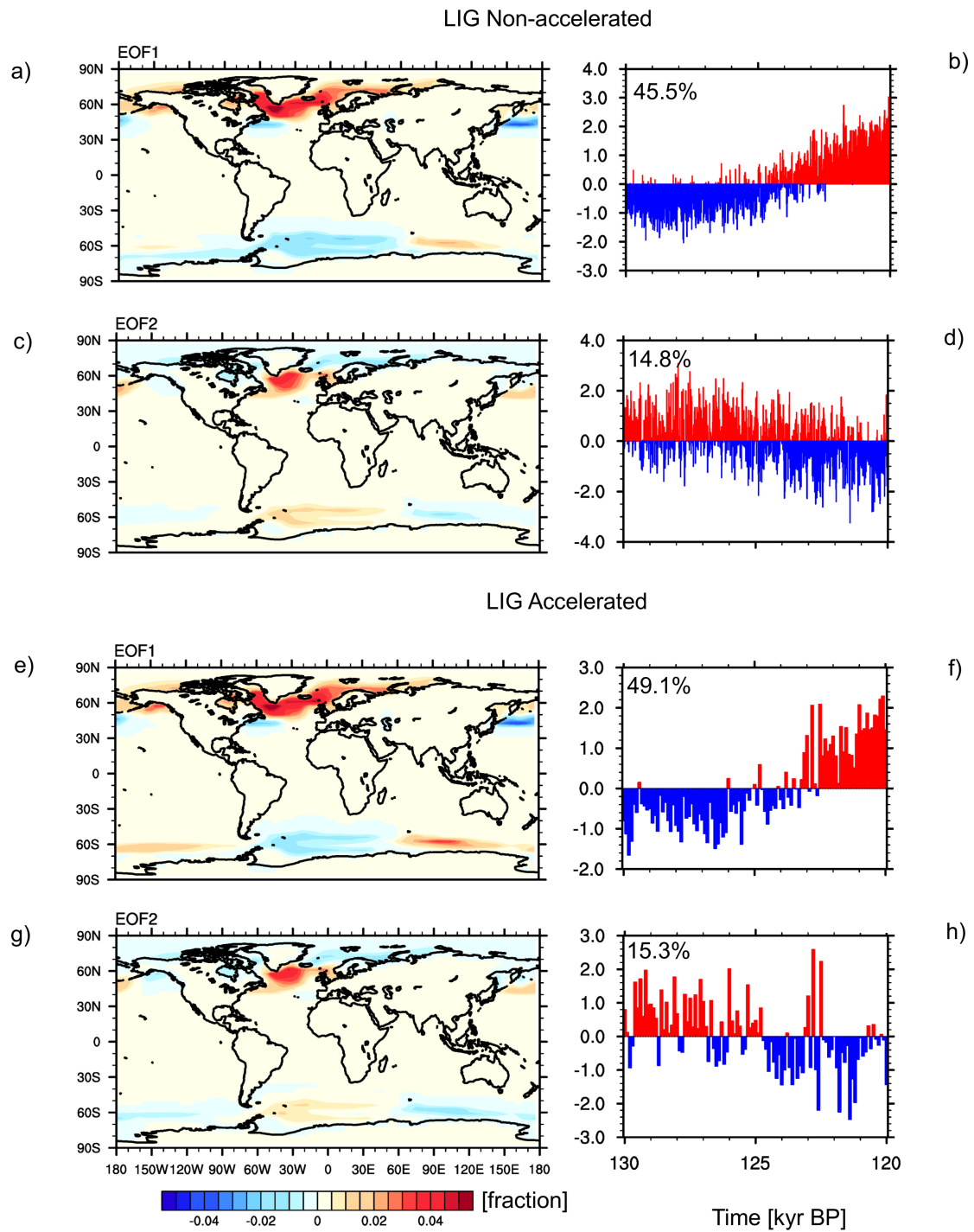
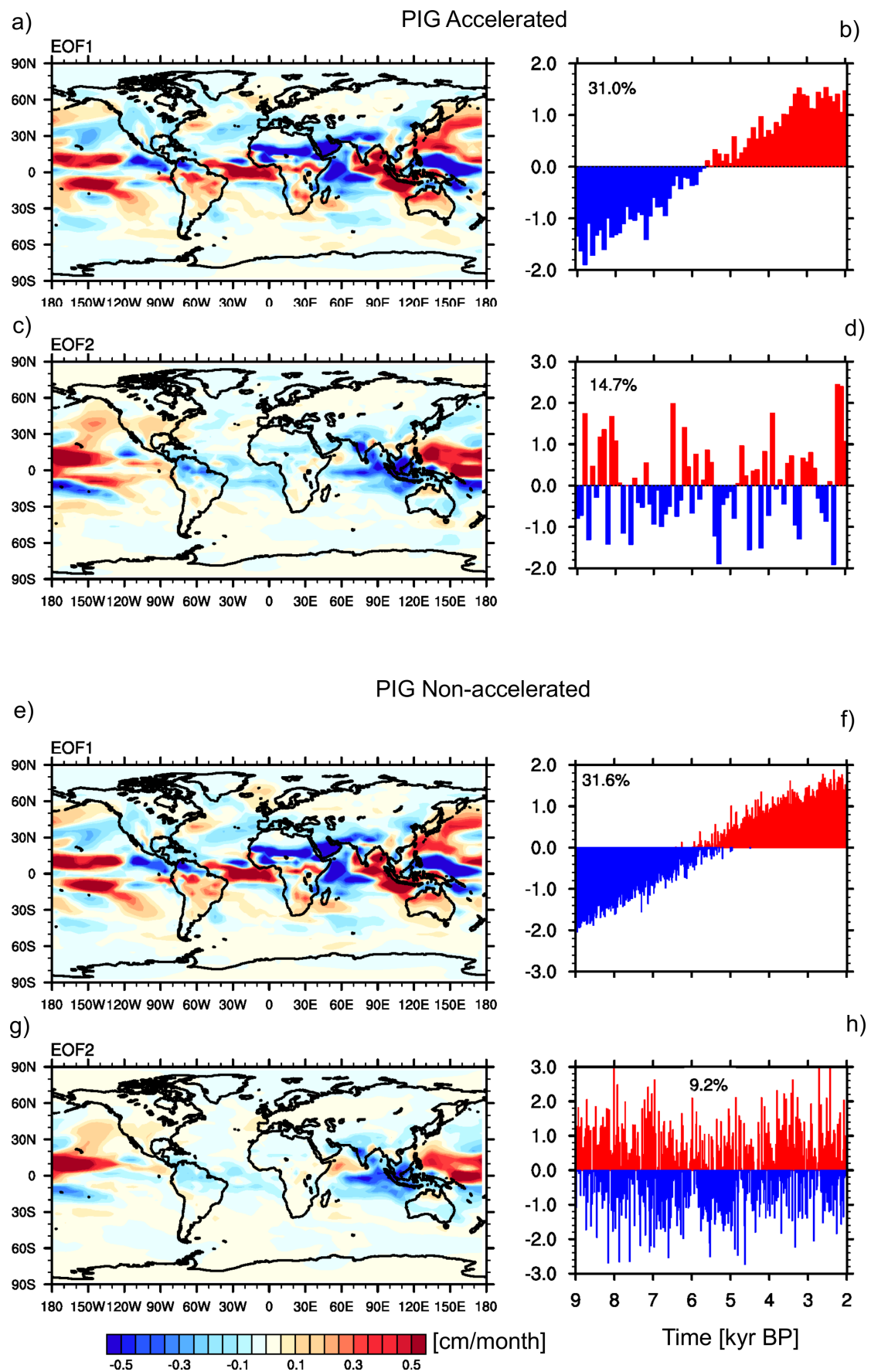Figure 8. Same as Fig. 5 but for LIG sea-ice concentration.

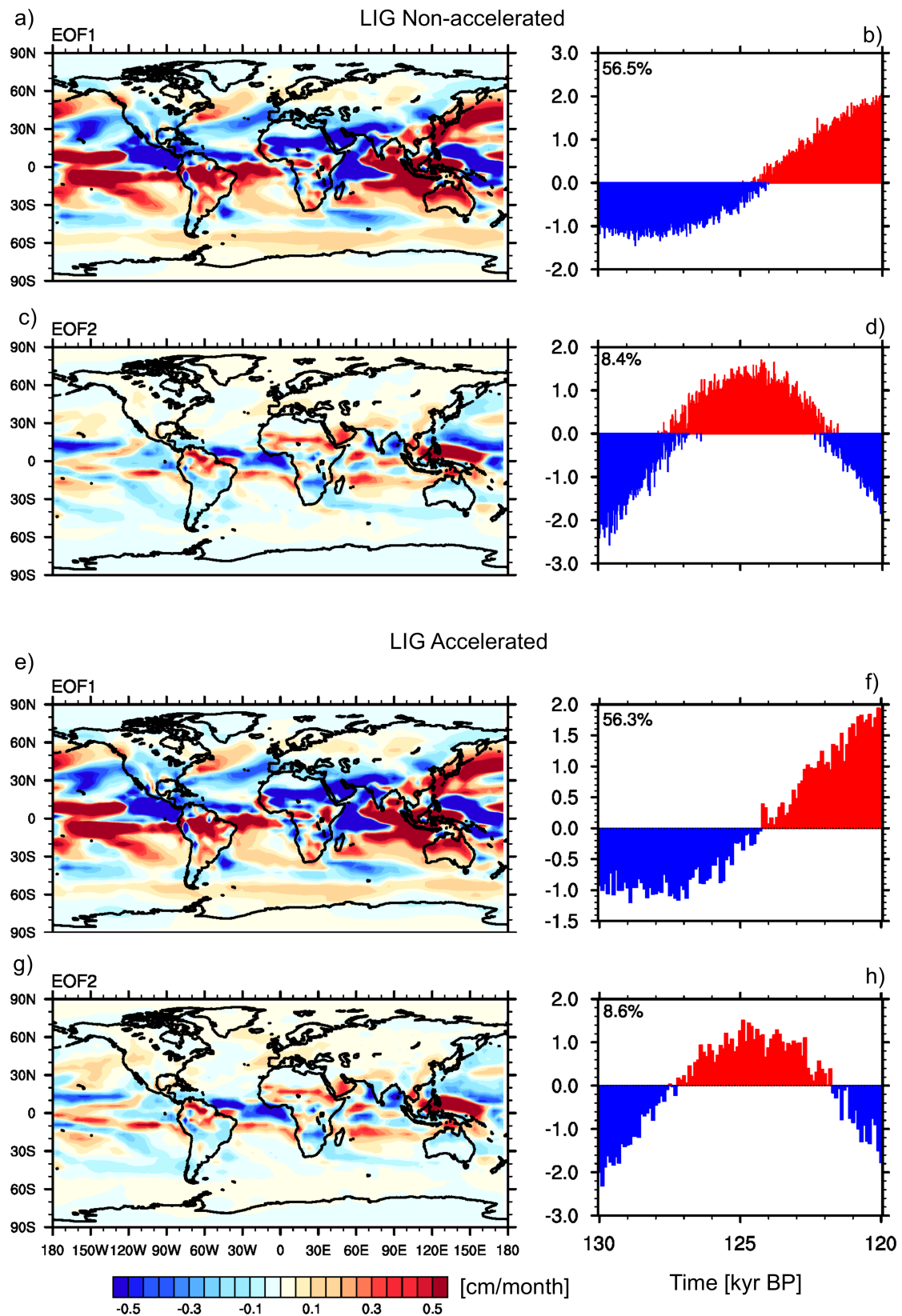Figure 9. Same as Fig. 5 but for PIG precipitation.
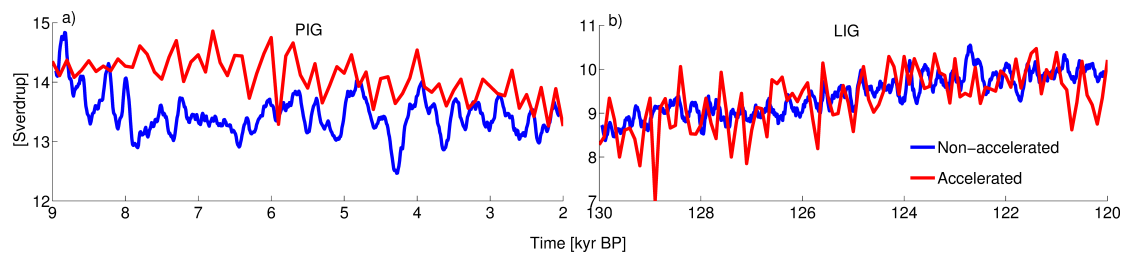
Figure 10. Same as Fig. 5 but for LIG precipitation.

624

625 Figure 11. Temporal evolution of the Atlantic Meridional Overturning Circulation
626 (given as the maximum of the North Atlantic overturning streamfunction) during both
627 the interglacials for both non-accelerated (blue) and accelerated (red) simulations. All
628 plots were created using the decadal mean values (referring to model years). In
629 addition, a 10-point running average was applied to the decadal mean values of the
630 non-accelerated simulations.

631

PIG : Accelerated minus non-accelerated (TS)

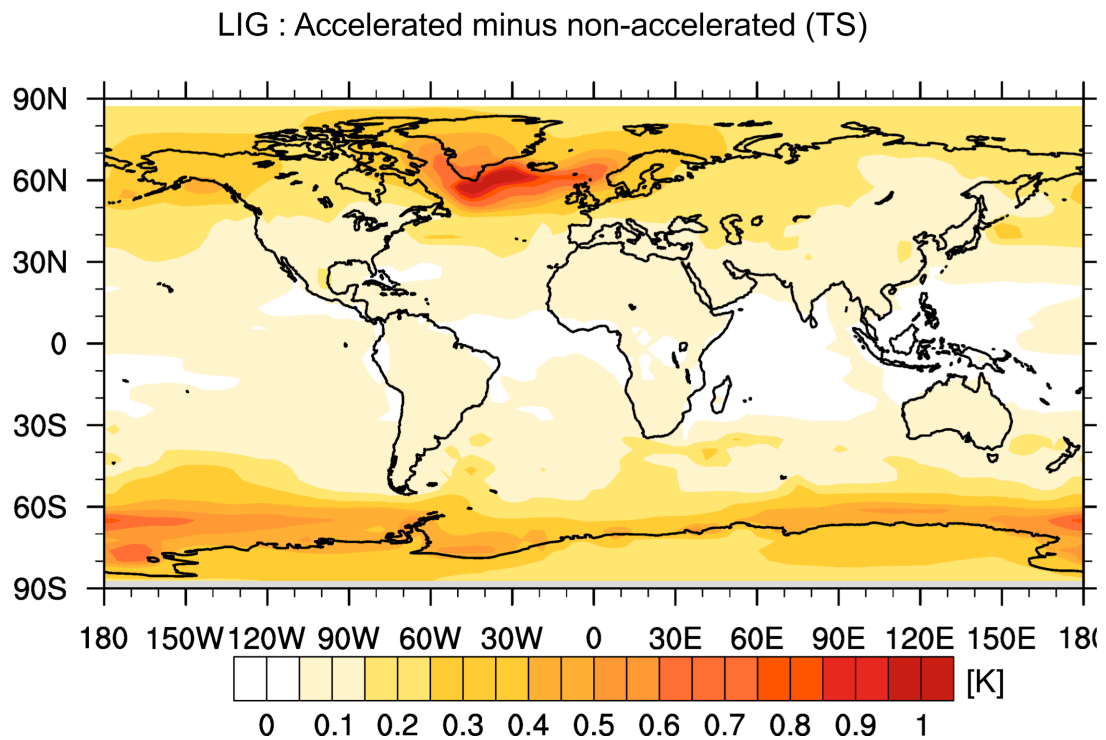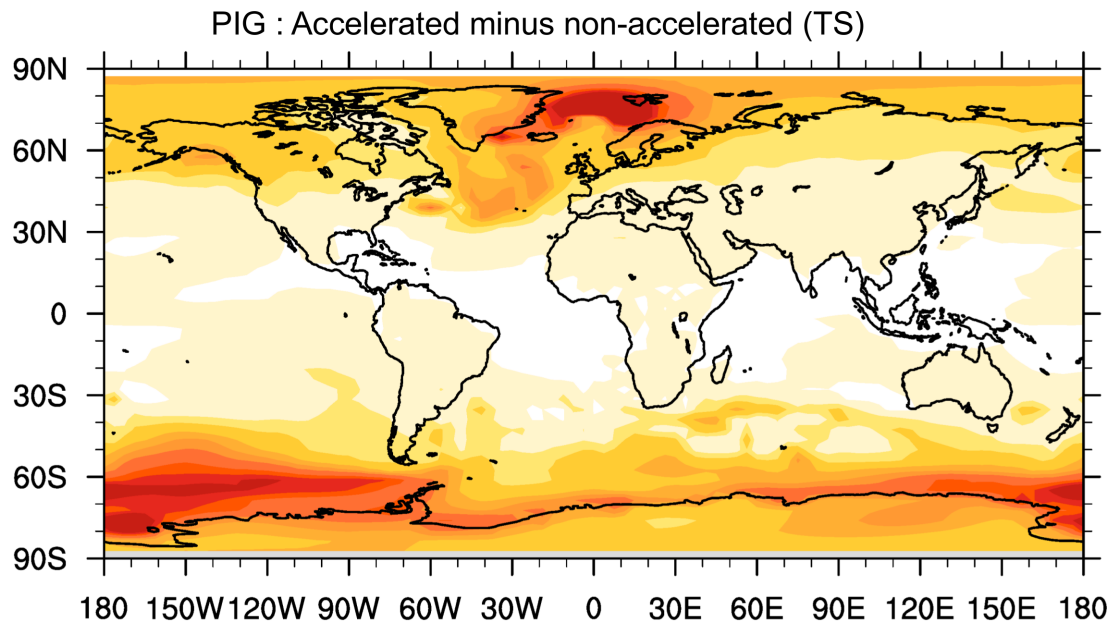LIG : Accelerated minus non-accelerated (TS)

Fig. 12. Root-mean-square difference between accelerated and non-accelerated simulations for surface temperature (TS). All plots were created using the decadal mean values (referring to model years). 10-year bins are used for the non-accelerated run to have the same number of data points on the time axis as in the accelerated simulation. An additional 1000 orbital year filter has been applied to both accelerated and non-accelerated time series to remove noise. Due to these low-pass filtering only

640   the long-term (orbital-forced) trend variability is considered by the root-mean-square

641   deviations.

642

643